國立臺灣大學理學院地理環境資源學研究所

碩士論文

Department of Geography
College of Science
National Taiwan University
Master's Thesis

以衛星影像與光譜混合分析方法監測大阿里山茶區之崩塌地

Landslide Detection Using Spectral Mixture Analysis and Satellite Imagery in the Great Ali-Mountain Tea Plantation Region in Southern Taiwan

沈姿雨

Zih-Yu Shen

指導教授：黃倬英 博士

Advisor: Cho-Ying Huang, Ph.D.

中華民國 114 年 7 月

July, 2025

doi:10.6342/NTU202504349

誌謝

首先，誠摯感謝指導教授黃倬英老師，從大專生計畫一路到碩士論文，老師不僅在學術上給予我細心的指導，更讓我深刻感受到對研究的熱忱與專注，這些都成為我寶貴的學習榜樣。

感謝陳慈忻學姊在土地使用分類上的指導與協助，讓我的研究能夠順利推進。感謝莊昀叡老師與王雪卿老師擔任我的口試委員，提供了許多關於遙測與崩塌地研究的寶貴建議；同時也感謝莊昀叡老師與蔡亞倫老師擔任我的預口試委員，對於研究方法與論文寫作給予我關鍵的回饋與方向。

感謝專題討論二的同學們，一起度過了許多充滿挑戰與歡笑的課堂時光。感謝 R605（原 R608）以及 R303 的同仁們長期的支持與鼓勵，特別是婉瑜、桔云、寶緯，總是在我哀哀叫的時候聆聽並陪伴我。

謝謝人豪、詠青、英綺、蘊盈、緒慈、懿修、郭昕、翰妤、丫春、沄芳、宇婕等朋友，經常提供我滿滿的情緒價值與陪伴聊天，讓我能在壓力中保持前進的動力，否則我很可能無法完成這篇論文。

感謝這兩年間照顧過我的所有醫生（雖然看診次數可能有點多），讓我在最後的關鍵時刻依然（大致上）保持健康。最後，感謝媽媽讓我能無後顧之憂地完成學業（雖然壓力還是不少），以及所有家人的支持與陪伴。

doi:10.6342/NTU202504349

中文摘要

臺灣山區的茶產業是重要的經濟活動，但過去研究指出，森林轉為茶園等土地使用變化，可能提升崩塌與土壤流失風險。然而，茶樹具有密集根系且多配備完善排水系統，也可能發揮穩定坡地的正面效果。本研究以大阿里山地區為對象，結合中高解析度衛星影像與空間分析技術，深入探討茶園是否對崩塌地發生具有顯著影響。首先，我們以 U-net 深度學習模型結合 Sentinel-2 多時序影像、數值地表模型與地面實測資料，進行土地使用分類，獲得高準確度（整體準確度與茶園的使用者/生產者準確度均超過 90%）的分類結果。接著，使用 Landsat 地表反射率影像進行 Bayesian MAP 光譜校正，確保多源影像的一致性，再以 AutoMCU 光譜混合分析法（SMA）推估崩塌地之土壤比例，建構跨年度的崩塌地分布圖。最後，透過環域分析（buffer analysis），計算不同土地使用類型周圍各距離範圍內之崩塌地面積與變化量。結果顯示，整體崩塌地面積在近 20 年間有下降趨勢。環域分析亦發現，茶園周圍 400 公尺內的崩塌風險相對較高，但其變化幅度不若森林明顯，且土壤比例變化速率在 400 公尺後趨於平緩，顯示其影響具有空間限制。整體而言，茶園並未導致明顯高於其他地類的崩塌風險，反而可能因管理設施而具有緩坡穩定的潛力。該結果有助於重新評估山地農業與地景穩定性之間的關係，並作為未來永續農業規劃的參考依據。

關鍵字：山地農業、耦合人類環境系統、光學遙測衛星影像、時間序列

doi:10.6342/NTU202504349

ABSTRACT

Tea cultivation is a key component of mountainous agriculture in Taiwan. While previous studies have suggested that land use changes—particularly forest conversion to tea plantations—may increase the risk of landslides and soil erosion, tea plantations also feature dense root systems and well-designed drainage infrastructure, potentially mitigating such hazards. This study investigates whether tea plantations contribute to landslide occurrence in the Greater Ali Mountain region by integrating remote sensing, spectral analysis, and spatial modeling. We first applied a U-net deep learning model to classify land use and land cover (LULC) using multi-season Sentinel-2 imagery, a digital surface model (DSM), and ground truth data. The resulting LULC maps achieved high classification performance, with overall accuracy and both user's and producer's accuracy for tea plantations exceeding 90%. To generate consistent surface reflectance values across Landsat imagery, we conducted Bayesian Maximum A Posteriori (MAP) spectral correction. Landslide mapping was then performed using the AutoMCU spectral mixture analysis (SMA) model, which estimates sub-pixel fractions of photosynthetic vegetation (PV), non-photosynthetic vegetation (NPV), and soil, enabling accurate landslide delineation based on elevated soil fractions. Buffer analysis was employed to assess the spatial distribution of landslide-prone areas around different LULC types. Results show that total landslide area has decreased steadily over the past two decades. While a higher landslide density was observed within 400 meters of tea plantations, the magnitude of change was less pronounced than that surrounding forests. The rate of change in soil proportion also declined beyond the 400-meter threshold, indicating spatially limited influence. These findings suggest that tea plantations do not

doi:10.6342/NTU202504349

significantly exacerbate landslide hazards and may, in some cases, contribute to slope stability. This research offers new insights into the complex relationship between mountainous agriculture and landscape hazards and provides a valuable reference for sustainable land management in hilly regions.

Key words: Agroecosystem, coupled human-environment system, optical remote sensing, time series

doi:10.6342/NTU202504349

CONTENTS

doi:10.6342/NTU202504349

doi:10.6342/NTU202504349

LIST OF FIGURES

doi:10.6342/NTU202504349

doi:10.6342/NTU202504349

LIST OF TABLES

doi:10.6342/NTU202504349

Chapter 1 Introduction

Landslides are one of the most destructive natural hazards globally, with far-reaching impacts on topography, ecosystems, infrastructure, and human well-being (Geertsema et al., 2009; Schuster & Highland, 2001). Geomorphologically, landslides reshape mountain slopes, river valleys, and even submarine landscapes (Geertsema et al., 2009; Vanneste et al., 2006), contributing to the long-term evolution of Earth’s surface. As Costa and Schuster (1987) observed, massive slope failures can block rivers and create unstable natural dams, which may lead to catastrophic downstream flooding if breached. Landslides also degrade water quality by introducing large sediment loads into rivers and reservoirs (Chen et al., 2006; Kelsey, 1978), which disrupts aquatic ecosystems and reduces water availability for agriculture and domestic use (Alimohammadlou et al., 2013). Ecologically, they strip forests and vegetation (Garwood et al., 1979), fragment habitats, and threaten biodiversity (Guariguata, 1990; Schuster & Highland, 2007)—particularly in tropical and mountainous regions (Alimohammadlou et al., 2013) (Garwood et al., 1979; Geertsema et al., 2009; Guariguata, 1990). According to Guariguata (1990), these impacts are often irreversible and can severely hinder natural regeneration.

Socioeconomic consequences are equally severe: landslides destroy homes (Chen et al., 2006; Knapen et al., 2006), agricultural lands, transportation routes, and lifelines such as power lines and water systems (Geertsema et al., 2009; Schuster & Highland, 2001). As noted by Alimohammadlou et al. (2013), landslides in urban or densely populated areas often lead to large-scale displacement, loss of livelihoods, and prolonged recovery periods. Significant events, such as the 1999 Vargas tragedy in

Venezuela (~30,000 deaths) (Schuster & Highland, 2001) or the 1970 Huascarán avalanche in Peru (~18,000 deaths) (Plafker et al., 1971), highlight the human cost of such disasters. In the United States, landslides result in $1–2 billion in annual losses and 25–50 deaths (Highland & Bobrowsky, 2008). In addition, Kjekstad and Highland (2009) noted that beyond direct damage, landslides can trigger substantial indirect consequences, including declining land value, loss of tax revenue, reduced tourism, and long-term psychological distress for affected communities. As climate change intensifies rainfall patterns and human development continues to expand into hazard-prone areas, landslides are becoming a growing concern across both developing and developed countries (Gariano & Guzzetti, 2016). Understanding how land use—particularly mountain agriculture—interacts with slope processes is therefore essential for managing landslide risk in vulnerable landscapes worldwide.

Mountain agriculture plays a dual role in sustaining rural livelihoods and shaping slope dynamics, often increasing the vulnerability of landscapes to landslides (Gu et al., 2019). Agricultural activities—such as land clearing, terracing, and deforestation (Garcia-Chevesich et al., 2021; Imaizumi et al., 2008; Persichillo et al., 2017)—frequently disturb natural vegetation cover and alter soil structure, leading to decreased root cohesion and increased susceptibility to surface erosion and mass movements. While Liu et al. (2024) emphasized its importance in enhancing productivity in arid and semi-arid regions, Gu et al. (2019) and Hou et al. (2018) pointed out that excessive or poorly managed irrigation methods—such as flood irrigation or leaky canals—can elevate groundwater levels and saturate soil layers, ultimately triggering slope failures. This phenomenon is notably observed in China's Loess Plateau (Gu et al., 2019; Hou et al., 2018), Peru's Andean valleys (Lacroix et al., 2020), and other regions where irrigation-induced landslides have become more frequent and severe (Garcia-Chevesich et al., 2021). Structural measures, such as slope stabilization and drainage, have been implemented; however, they often fail to address the root cause—excessive water infiltration. As agriculture continues to expand into fragile mountainous terrains, particularly to meet the rising demand for high-value crops, understanding how specific land uses contribute to slope instability is essential. Among these crops, tea stands out—not only as a culturally significant beverage but also as a global commodity whose cultivation increasingly concentrates in sensitive highland regions.

Tea is the second most consumed beverage in the world after water (Wu & Wei, 2009), making it both culturally significant and economically valuable. Global demand for tea continues to grow (FAO, 2022; Statista, 2025), especially for premium varieties that offer unique flavor profiles and health benefits (Dou, 2019; Xu et al., 2012). Among these, high-mountain tea holds particular importance due to its distinctive quality and higher market price (Chen et al., 2010; Han et al., 2016; R. Wang et al., 2018). Grown at elevations typically above 1,000 meters, high-mountain tea is prized for its smoothness, reduced bitterness, and floral aroma, characteristics influenced by cooler temperatures, slower leaf growth, and higher humidity (Chen et al., 2025; R. Wang et al., 2018). Scientific studies have shown that lower catechin content and higher amino acid concentration in tea leaves—both conditions favored by high-altitude environments—are associated with better taste and higher quality (Han et al., 2016), making such teas more competitive in international markets. As a result, the cultivation of high-mountain tea plays a vital role in the global tea industry, both in terms of economic return and branding potential for tea-producing regions.

Taiwan’s high mountain regions, characterized by steep slopes, frequent rainfall, and dynamic geological activity (Chen et al., 2007; Yanites et al., 2018), are home to some of the world's most renowned high-mountain teas (Chen et al., 2025). These areas, often located above 1,000 meters in elevation, provide the ideal microclimate—cool temperatures, mist, and well-drained soils—for cultivating premium tea with rich aroma and smooth flavor (Han et al., 2017; Ren et al., 2025; R. Wang et al., 2018). However, cultivating tea in such environments requires considerable investment. As Papaskiri et al. (2019) noted, the development of high-mountain plantations involves not only the cost of land acquisition but also the construction of terraces, retaining structures, irrigation systems, and access roads, rendering it a capital-intensive enterprise. This financial commitment incentivizes farmers to preserve slope stability and implement long-term conservation measures. With careful site selection, proper drainage planning, and sustainable land management practices, high-mountain tea cultivation does not inherently lead to landslides (Haq & Boz, 2018). Instead, when responsibly managed, tea plantations can coexist with the mountain landscape, emphasizing the importance of regulatory oversight and ecological planning in minimizing environmental impact.

Given the ecological and economic significance of high-mountain tea cultivation in Taiwan, it is crucial to examine its relationship with landslide susceptibility critically. While tea plantations are often situated in geologically sensitive areas, their development typically involves substantial investment and infrastructure, which encourages responsible land management. With proper site selection and sustainable practices, tea farming does not inherently increase landslide risk. Nevertheless, the potential spatial interactions between plantation distribution and slope instability remain underexplored. Therefore, this study aims to (1) classify land cover using machine learning methods, (2) detect and map landslides using spectral unmixing analysis, and (3) evaluate the spatial relationship between tea plantations and landslide occurrence in Taiwan's high mountain regions.

doi:10.6342/NTU202504349

Chapter 2 Methods

2.1 Study area

The study area is the Greater Ali Mountain (Ali-Shan) tea production region, encompassing Zhuxi, Fanlu, Meishan, and Alishan Townships in Chiayi County, Taiwan (Figure 1). Among these, Meishan Township has the earliest records of tea cultivation, dating back to the Japanese colonial period. However, significant expansion of tea plantations did not occur until the 1980s, when cultivation began to spread along the Alishan Highway into other parts of the Greater Ali Mountain area. After 2000, the total area of tea cultivation has remained relatively stable (as shown in Figure 1-d).

The elevation of the Greater Ali Mountain tea region ranges approximately from 800 to 1500 meters above sea level. The area is characterized by persistent cloud cover and cool high-mountain climate conditions, which are favorable for tea cultivation (Huang, 2013). As of 2022, the total tea plantation area in the region reached 1,750 hectares, accounting for about 14.3% of Taiwan’s total tea cultivation area. The region produced 1,825 metric tons of tea, accounting for 13% of the nation’s total tea harvest, making it one of the most significant mountain tea-producing areas in Taiwan.

To analyze the relationship between tea plantations and landslides in adjacent areas, this study defines the spatial extent of the study area to include elevations ranging from 700 to 1,600 m asl covering 36936 ha of the mountains. Since remote sensing is a powerful tool for both land use/land cover (LULC) classification and landslide monitoring over a vast region (Digra et al., 2022; Khatami et al., 2016; Zhao & Lu, 2018), this study adopts satellite imagery as the primary data source. The use of medium-resolution multispectral data enables consistent, large-area coverage across complex terrain, making it particularly suitable for mountainous regions like the Greater Ali-Mountain area. By integrating spectral, spatial, and temporal information, remote sensing provides an efficient means to detect surface changes over time, classify land use patterns, and identify landslide-prone zones with greater precision than traditional field-based approaches.

2.2 Image processing for land use classification

This study utilized Sentinel-2 imagery from 2019 to 2021, which was seasonally categorized and primarily comprised visible, near-infrared (NIR), and shortwave infrared (SWIR) bands. Sentinel-2 offers spatial resolutions of 10 meters (for visible and NIR) and 20 meters (for shortwave infrared), which are suitable for capturing the spatial scale of tea plantations. Although Sentinel-2A/B have minor differences in band center wavelengths, their spectral ranges are similar, and both are onboard the same type of sensor, making them reliable sources for long-term monitoring. Appendix A provides a comparison of the observation bands and sensors of the Sentinel-2 series satellites. All Sentinel-2 imagery used in this study was obtained from Google Earth Engine (Gorelick et al., 2017) and derived from atmospherically corrected surface reflectance products (Level-2A).

For elevation data, the study utilized the ALOS DSM: Global 30m v3.2 dataset, available in Google Earth Engine, which provides 30-m resolution elevation information, supplementing topographic parameters within the study area. Since most of the field reference data used in this study were collected in 2020, Sentinel-2 imagery from 2020 was prioritized, with data from the adjacent years (2019 and 2021) used to fill in data gaps. In the preprocessing phase, cloud-covered pixels were identified and masked using the QA60 band in Sentinel-2 imagery. For each pixel, the 40th percentile of all valid observations was calculated across bands to reduce the influence of outliers. If missing values remained after this step, a focal mean was applied using surrounding pixels until all missing values were filled.

Because the signal strength and numerical range of different bands may vary (e.g., red band reflectance ranges from 0 to 0.4 vs. NIR from 0 to 0.7), the model may overweight bands with greater variance during training. To mitigate this, band values were standardized. The imagery was divided into four seasonal composites: spring (March–May), summer (June–August), autumn (September–November), and winter (December–February). We processed each seasonal image using cloud masking, 40th percentile computation, and gap filling. To ensure consistent value ranges across seasons, the 0.5th and 99.5th percentiles of each band were used to normalize seasonal images throughout the entire year. We rescaled red band values in all seasonal composites based on the annual red band's 0.5th to 99.5th percentile range. Therefore, the final image values may not necessarily fall between 0 and 1, but are adjusted according to the characteristics of each band.

2.3 Convolutional neural network model

This study employed the U-Net model (Ronneberger et al., 2015) for land use classification. U-Net is well-known for its capability in semantic segmentation, allowing for the extraction of fine-grained spatial features and textures. By incorporating contextual information from neighboring pixels, U-Net enhances classification accuracy and performance in heterogeneous landscapes. Prior to training, Sentinel-2 images were divided into smaller patches to serve as input data. The dataset

doi:10.6342/NTU202504349

was split into training and validation subsets in a 60:40 ratio, ensuring that model parameter tuning did not affect final validation outcomes. To improve the model's generalization ability, we applied data augmentation techniques to the training set, including horizontal and vertical flipping, as well as random rotations. These augmentations helped the model recognize the same land cover features under varied orientations.

The model architecture was built using Keras with a TensorFlow backend, and ResNet-18 (He et al., 2015) was used as the encoder backbone. Based on model performance tests, training stabilized after approximately 40 epochs. Therefore, we ran each training session for 50 epochs to ensure convergence and optimal results. All model training and evaluation were conducted on Google Colaboratory (Colab), which provided GPU-accelerated computing resources and a flexible Python-based environment suitable for deep learning development.

2.4 Ground truth data for land use classification

To train the U-Net model, this study converted ground truth data into raster format and further divided it into training and validation datasets. The ground truth data for tea plantations were manually interpreted and digitized from aerial photographs provided by the Forestry and Nature Conservation Agency's Aerial Survey and Remote Sensing Branch under the Ministry of Agriculture. For the remaining land use types, data were based on the National Land Use Survey conducted by the National Land Surveying and Mapping Center, followed by manual digitization and verification.

Land use in the study area was categorized into five classes: forest, bare soil, tea plantation, cropland, and impervious surface. During preprocessing, we rasterized the

doi:10.6342/NTU202504349

polygon data and adjusted the number of pixels assigned to the training and validation sets to meet the model's requirements. Efforts were made to maintain a balanced number of samples across land use classes to prevent model bias due to class imbalance. The processed data were saved in GeoTIFF format and used for model training and evaluation on **Google Colaboratory (https://colab.research.google.com/)**.

2.5 Model performance evaluation

To evaluate the classification performance of the U-Net model, this study adopted two complementary approaches:

(1). Validation accuracy assessment: For each classification result, 80% of the validation dataset was randomly sampled and used to calculate classification accuracy. This process was repeated 20 times to obtain the average and standard deviation of the results. Given that tea plantations and forests are the most frequently confused classes, model evaluation focused on overall accuracy (OA), as well as the user's accuracy (UA) and producer's accuracy (PA) for both tea plantations and forests.

(2). Model stability assessment: The U-Net model was trained ten times independently, and accuracy metrics were recorded for each run. The standard deviation of OA, UA, and PA was used to assess model stability and robustness. A model with higher mean accuracy and lower variation across runs was considered more reliable and effective for land use classification in the study area.

doi:10.6342/NTU202504349

2.6 Landslide analysis

This study utilized Landsats satellite imagery for landslide analysis, primarily using the blue, green, red, NIR, and SWIR bands. All imagery was obtained from Google Earth Engine (Gorelick et al., 2017) and selected from surface reflectance products that have undergone atmospheric correction to ensure data consistency and comparability. The Landsat imagery used in this study comes from Level-2, Collection 2 datasets. Level 2 indicates that atmospheric correction has been applied, while Collection 2 offers improved cloud classification and provides cloud shadow confidence scores, thereby enhancing the precision of image filtering.

Since Landsat 7 imagery has suffered from Scan Line Corrector (SLC) failure since 2003, resulting in image striping (https://www.usgs.gov/landsat-missions/landsat-7), this study only used Landsats 5, 8, and 9 imagery. Table 4 summarizes the sensor and spectral characteristics of different Landsat satellites.

Considering that mountainous regions are often covered in clouds, this study selected winter-season images (December to January) with minimal cloud cover for analysis. A single cloud-free image was chosen for spectral analysis to maximize precision and stability.

Since this study used fixed spectral endmember values while satellite imagery is susceptible to atmospheric variation, a calibration procedure was implemented to harmonize imagery across other years. As a result, the study adopted the method proposed by Che et al. (2021), which uses MODIS as a stable reference. A regression model was built between MODIS and Landsat imagery for the same regions, enabling inter-annual spectral calibration and improving consistency across years. Specifically,

doi:10.6342/NTU202504349

MODIS Nadir BRDF-Adjusted Reflectance Daily 500m (MCD43A4.061) was used as the reference dataset. This product combines data from Aqua and Terra satellites and selects the most representative pixels within a 16-day window, ensuring temporal continuity and stability.

To improve the spectral consistency of Landsat imagery from different years and sources, this study applied MODIS BRDF-based correction to align Landsat reflectance more closely with MODIS standards. For each band and region, a Bayesian regression model was constructed with MODIS BRDF values as the target reflectance and original Landsat reflectance as predictors. The model was implemented in Python, with a prior distribution of 0.01 (sensitivity tests between 0 and 1 showed little difference), which controls the degree of adjustment and prevents overfitting. The posterior mean was used as the corrected Landsat reflectance, which was then used for subsequent AutoMCU spectral unmixing and landslide interpretation.

This correction strategy effectively combines the temporal stability of MODIS with the spatial resolution of Landsat, enhancing the spectral consistency of multi-source imagery and ensuring the feasibility and accuracy of multi-temporal comparisons.

2.7 Spectral mixture analysis method

This study employed AutoMCU (Automated Monte Carlo Unmixing) for spectral mixture analysis, taking into account the complex surface composition and high vegetation coverage in the mountainous study area. The land surface was classified into three major endmembers: photosynthetic vegetation (PV), non-photosynthetic vegetation (NPV), and bare soil. By estimating the spectral proportion of PV, NPV, and soil within each pixel, we were able to assess vegetation conditions and identify potential landslide occurrences. Endmembers refer to the pure spectral signatures of surface components, such as leaves for PV and branches for NPV.

Prior to implementing AutoMCU, an endmember spectral library must be established. This study utilized the dataset compiled by Huang et al. (2013), which included NPV and soil spectra collected from various forested sites across Taiwan using a portable spectroradiometer. The spectra span from 350 to 2500 nm with a 1 nm resolution. Given the high canopy structure of Taiwan’s forests, direct measurement of PV spectra is challenging; therefore, this study utilized Hyperion hyperspectral imagery (Ungar et al., 2003) to extract PV endmembers. Hyperion covers a spectral range of 426.82 to 2395.50 nm with a resolution of 10–12 nm. The resulting spectral library contains 550 PV samples, 269 NPV samples, and 256 soil samples (Huang et al., 2013). Before analysis, all spectra were resampled to match the spectral bands of Landsat to ensure compatibility.

After preprocessing, AutoMCU analysis was performed. Endmembers were randomly selected from each category, and each pixel's reflectance was modeled as a mixture of these endmembers based on the following formula (Asner & Lobell, 2000):

$$\rho_{pixel}=\sigma[\rho_{e}\cdot C_{e}]+\varepsilon=[\rho_{veg}\cdot C_{veg}+\rho_{soil}\cdot C_{soil}+\rho_{litter}\cdot C_{litter}]+\varepsilon \quad (1)$$

Here, ρ denotes the observed reflectance for each pixel in the satellite imagery, C represents the fraction of each endmember, and ε is the root mean square error (RMSE). The sum of C must equal 1. The outcome is the proportion of PV, NPV, and soil for each pixel.

To improve analytical stability, the endmember selection process was repeated 50 times per pixel, and the average and standard deviation of the proportions were computed. This entire procedure was repeated five times. If the standard deviation exceeded a predetermined threshold, indicating unstable sampling, the process was

doi:10.6342/NTU202504349

re-run to ensure data reliability. The AutoMCU analysis was primarily conducted on Google Colab, with code development in Visual Studio Code (Microsoft, 2024). Spectral data processing utilized GDAL (GDAL/OGR contributors, 2024), and matrix computations were handled using Eigen (Guennebaud et al., 2010).

2.8 Relationships between tea plantations and landslides

Following the AutoMCU analysis, this study used the proportion of the soil endmembers as an indicator. It employed buffer analysis as an exploratory spatial analysis method to evaluate whether tea plantations exhibit higher surrounding landslide proportions compared to other land use types. To capture spatial clustering of landslides across different scales, buffer distances were set from 10 to 1000 m, with an interval of 30 m. For each buffer zone, the proportion of landslides per unit area was calculated. The slope of change in landslide proportion across distances was then derived by applying the first derivative to the landslide proportion array, enabling a more precise representation of how landslide area and proportion vary with distance.

As the study area is primarily composed of forests, tea plantations, and impervious surfaces, the buffer-based landslide proportions among these three land use types were further compared to preliminarily assess whether tea plantation edges are associated with higher landslide risks. Prior to buffer analysis, areas classified as tea plantations and river channels were excluded to minimize external influence from other land use types or exposed riverbeds that could bias the results.

In addition, 2021 aerial imagery was manually interpreted to delineate landslide polygons, which were then used to set the soil fraction threshold indicative of landslide occurrence. This threshold was applied to AutoMCU outputs for multiple years to compare landslide extent across land cover categories and time periods, thereby providing a basis for evaluating their spatial relationships.

Buffer construction and statistical analysis were performed using the R programming language (R Core Team, 2024). Pearson's correlation coefficient was used to evaluate the strength of association between buffer distances and the proportion of landslide coverage. To further account for spatial heterogeneity potentially caused by topographic factors (e.g., slope and aspect), subsequent analyses incorporated slope classification to investigate whether the spatial relationship between tea plantations and landslides varies across different slope conditions.

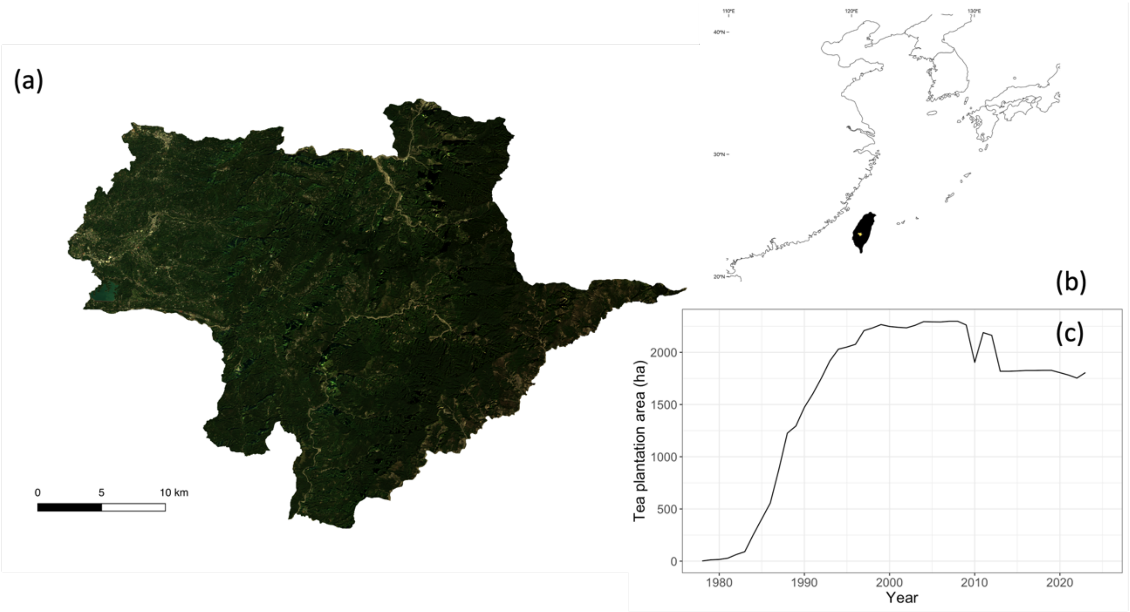

Figure 1. (a) True-color composite of the study area—the Greater Ali Mountain tea plantation region—derived from Sentinel-2 surface reflectance imagery (10 m spatial resolution) acquired on January 16, 2020. (b) The geographic location of the study area in Taiwan is highlighted in yellow. (c) The figure illustrates the changes in the tea plantation area in the Greater Ali Mountain region. A significant expansion is observed

around the 1980s, followed by a relatively stable trend after approximately the year 2000 (Council of Agriculture, 2024).

doi:10.6342/NTU202504349

Table 1. This table lists the acquisition dates of satellite imagery used in the AutoMCU-based spectral mixture analysis. Data were collected from four satellite platforms—Landsat 5, Landsat 8, and Landsat 9—spanning from 2005 to 2024. For each image, the acquisition date is shown along with the corresponding analysis year in parentheses. These multi-temporal datasets support long-term landslide detection and surface change monitoring in the study area.

Satellite Platform	**Image Acquisition Date (Used Year)**
Landsat 5	2005/01/20 (2005)
	2009/01/15 (2009)
	2010/01/18 (2010)
	2010/12/20 (2011)
Landsat 8	2014/01/29 (2014)
	2018/01/24 (2018)
	2019/12/13 (2020)
	2021/01/16 (2021)
Landsat 9	2023/01/30 (2023)
	2023/12/17 (2024)

Chapter 3 Results

3.1 Land use and land cover

The ground truth data were categorized into five land cover types and distributed across the study area. To ensure balanced representation for each category, some of the crop and impervious surface samples were collected from locations outside the four target counties (Figure 2).

This study employed seasonally composited Sentinel-2 imagery, along with a U-Net deep learning model, to perform land-use classification. The model was trained and validated 20 times using manually digitized ground truth points. Overall classification performance was high, and the model demonstrated strong consistency across different validation splits.

The land use classification results for the Greater Ali Mountain tea plantation region reveal accurate delineation of all five land cover classes, including tea plantations and forests (Figure 3). These two classes are particularly challenging to differentiate due to their similar spectral signatures in mountainous environments, yet the model effectively separated them. The classification accuracy for each class remained high, with user's and producer's accuracy consistently exceeding acceptable thresholds.

In summary, the combination of seasonally composited Sentinel-2 data and the U-Net model provides a robust approach for land use classification in mountainous areas. This method is particularly effective for mapping sloped landscapes that feature a mix of agricultural and forested areas.

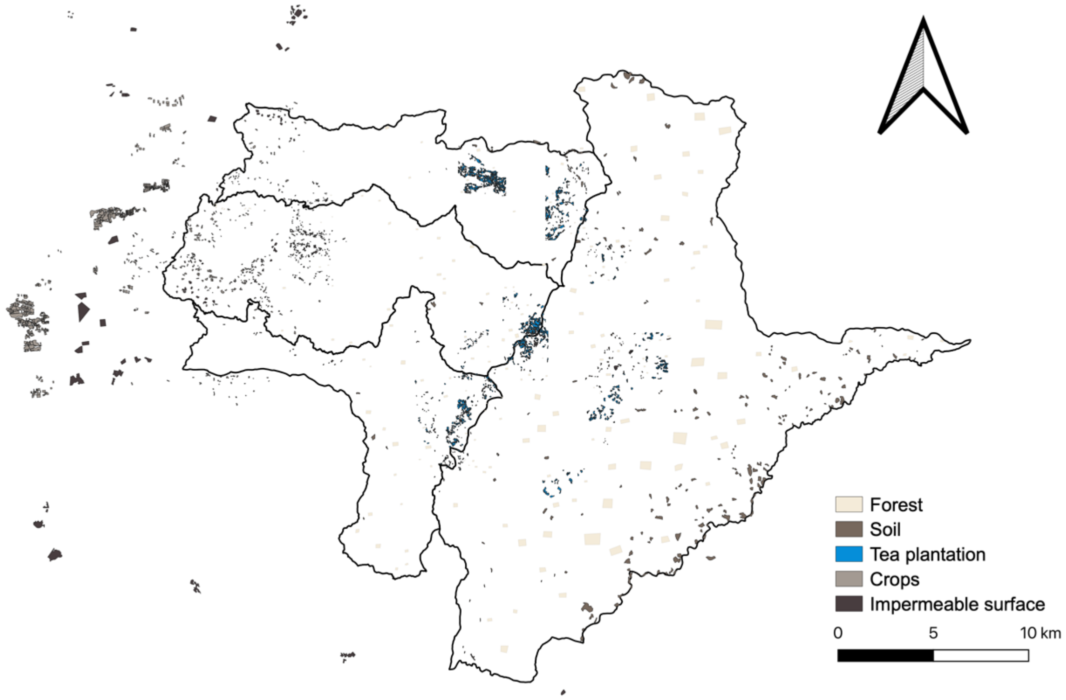

Figure 2. Colored areas within the study region indicate the locations where ground truth data are available. For the "Crops" and "Impervious Surfaces" categories, due to insufficient coverage within the Greater Ali Mountain tea region, some of the data were collected from areas outside the study site.

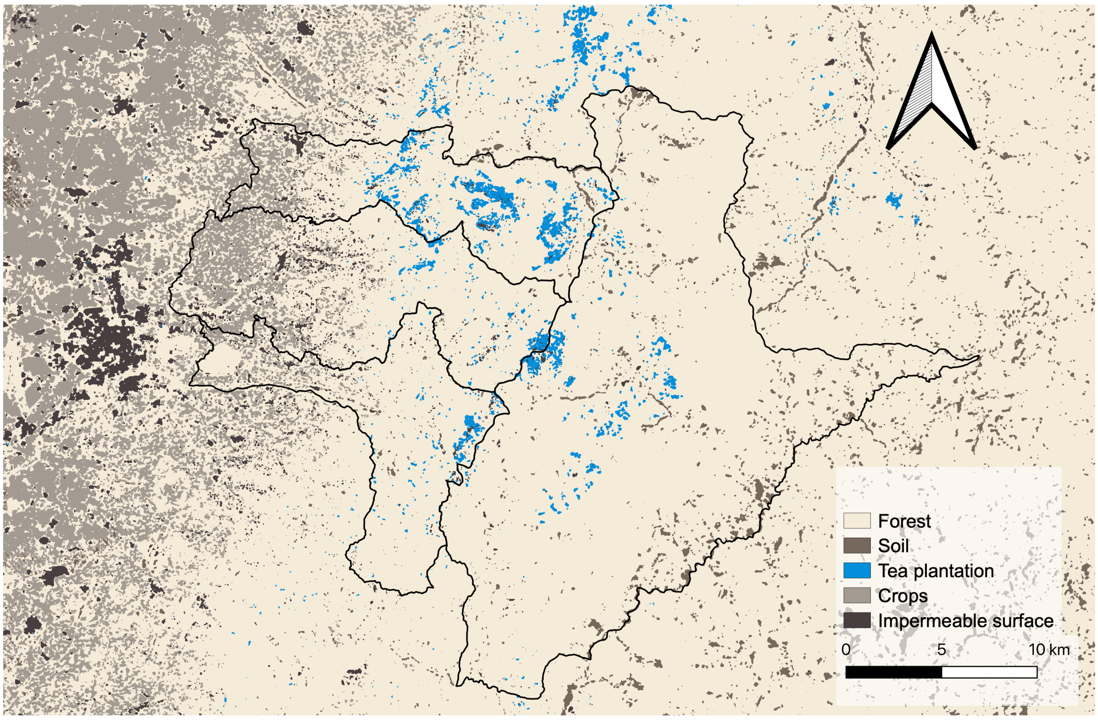

Figure 3. The white polygon delineates the boundary of the Greater Ali Mountain tea region. The map has a spatial resolution of 10 meters. As shown, the dominant land use within the study area is forest, while tea plantations are primarily concentrated along Provincial Highway 18 (the Alishan Highway).

Table 2. The OA achieved by the U-Net model was 0.944, with a standard deviation of only 0.005, indicating high classification stability. In terms of classification metrics, the UA and PA for all five land cover types exceeded 0.84, demonstrating the model's strong capability in distinguishing diverse landscape features.

Accuracy	**Forest**	**Soil**	**Tea plantation**	**Crops**	**Impermeable Surface**
UA avg	0.923	1	0.916	0.991	0.921
UA std	0.007	0	0.043	0.005	0.019
PA avg	0.997	0.849	0.939	0.882	0.861
PA std	0.002	0.035	0.037	0.012	0.052
	OA				
avg	0.944				
std	0.005				

3.2 Uncalibrated AutoMCU Analysis Results

The distribution of PV, NPV, and Soil endmembers across the Greater Ali Mountain tea plantation region was estimated using the AutoMCU method for nine selected years between 2005 and 2024 (Figure 4). Imagery was from Landsats 5 (2005 to 2011), 8 (2014 to 2021), and 9 (2022 to 2024). All input imagery was processed using basic atmospheric correction and AutoMCU unmixing, without applying inter-sensor spectral calibration.

The temporal patterns reveal a general decline in the Soil endmember (in red), suggesting a reduction in bare or landslide-prone surfaces over time. In contrast, green areas representing PV coverage show a gradual increase, particularly after 2020, which may reflect vegetation regrowth, ecological restoration, or the expansion of tea plantations. In specific years, such as 2009 and 2010, an abrupt concentration of red pixels is evident in the northern portion of the study area, likely indicating extensive landslide activity or bare surface exposure, potentially caused by typhoons or seismic events. This interpretation will be further explored in later sections.

It is essential to note that, due to differences in sensor characteristics and the lack of spectral calibration across years, some level of interannual bias may still be present. To address this, future work will incorporate spectral normalization techniques based on temporally stable reference pixels, enhancing the comparability of multitemporal analyses.

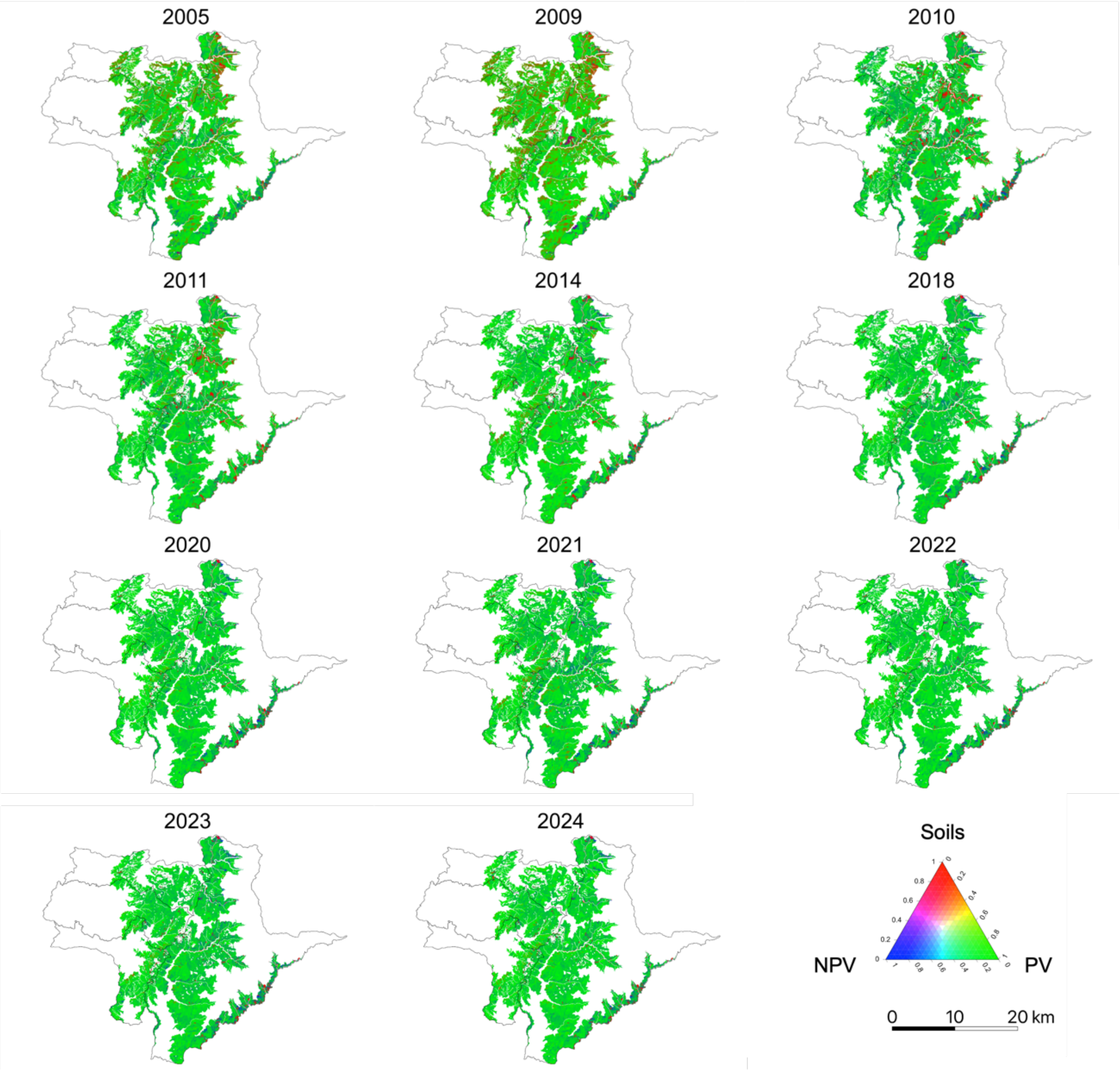

Figure 4. Tea plantations and river channels have been excluded from the analysis. The figure reveals a noticeably higher presence of landslide areas in 2009 and 2010, which may be attributed to the impact of typhoons that passed through the region during the

summer of the preceding year.

3.3 AutoMCU Analysis Results After Spectral Calibration

These observations suggest that while calibration using stable reference pixels can enhance temporal consistency, it may still introduce biases in certain years or locations. Limitations such as the representativeness of calibration targets or variability in image quality remain potential sources of error. Future improvements could involve expanding the number of calibration targets or incorporating alternative methods, such as harmonization or the use of pseudo-invariant features.

To further enhance inter-sensor consistency, this study applied a cross-sensor spectral correction method. MODIS and Landsats 5, 8, or 9 imagery acquired on matching dates were used to construct linear regression models for spectral conversion, based on band-wise correlation coefficients (R^2). These regression models were then used to adjust the spectral values of Landsat imagery, thereby minimizing biases caused by sensor differences and acquisition timing, and improving the temporal consistency of the AutoMCU analysis.

Using this approach, the corrected AutoMCU results show reduced inter-annual variability, suggesting improved temporal coherence (Figures 4 and 5). Nevertheless, areas affected by landslides still exhibit elevated soil proportions (red), indicating that the calibration preserved fundamental surface changes relevant to landslide detection.

doi:10.6342/NTU202504349

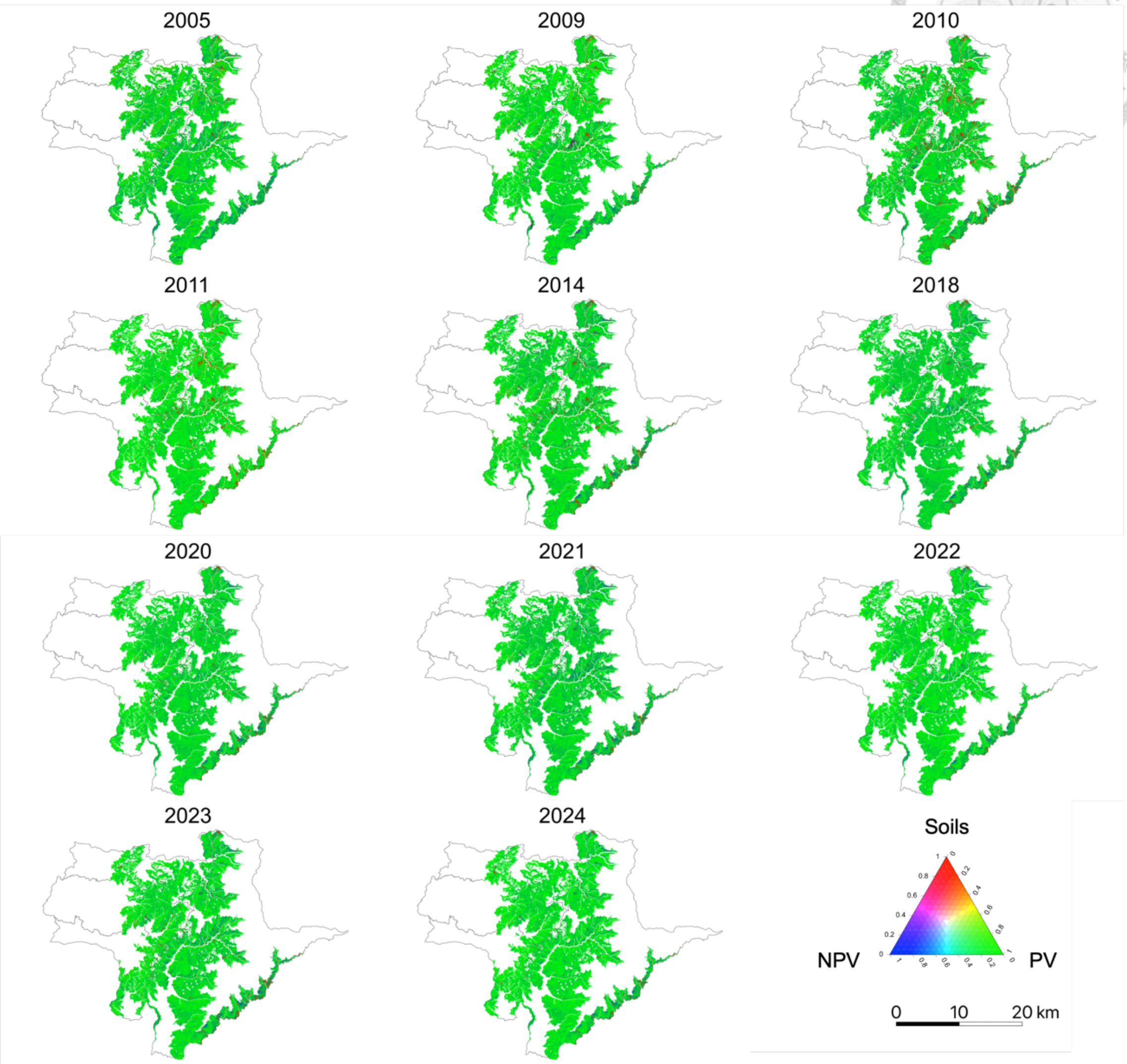

Figure 5. The AutoMCU result conducted by Landsats 5 (2005 to 2011), 8 (2014 to 2021), and 9 (2022 to 2024). Compared to Figure 5, the inter-annual variation is noticeably reduced, indicating improved consistency. However, distinct changes can still be observed in 2009 and 2010, reflecting the occurrence of landslides during those years.

3.4 Buffer Analysis of Landslide Distribution Across Different Land Use Types

This study employs buffer analysis to examine the spatial relationship between landslide distribution, represented by the soil endmember, and three major land use types: tea plantations, impervious surfaces, and forests. Buffers were created at 10-meter intervals, ranging from 10 to 1000 meters. Within each distance zone, the total soil area and the proportion of landslides were calculated based on the fractional soil content derived from AutoMCU. The total estimated soil area within each buffer is shown in the top row, while the first derivative (i.e., rate of change with distance) appears in the bottom row (Figure 6). The relative proportion of landslides normalized by total buffer area is presented as a spatial trend across distance from each land use type (Figure 7). Changes in landslide extent over time within 10-meter buffers are compared for different land use categories, revealing temporal variation in landslide activity (Figure 8).

The spatial distribution patterns indicate that landslides occur more frequently in proximity to tea plantations and forests than to impervious surfaces (Figure 6). Peak landslide activity is observed in 2009 and 2010, which aligns with extreme rainfall events such as Typhoon Morakot. Notably, tea plantations exhibit a rapid increase in total landslide extent within the first 400 meters, peaking around 350 meters, suggesting a strong spatial correlation between tea cultivation and adjacent slope failure. Forests display a similar but less pronounced pattern, with peak values between 250 and 300 meters. In contrast, impervious surfaces exhibit no clear spatial trend in landslide distribution.

The first derivative of landslide proportions is mostly negative across all land use

doi:10.6342/NTU202504349

types, indicating that landslide occurrence generally decreases with increasing distance from the land use feature (Figure 7, lower panels). This declining trend becomes more gradual beyond 400–500 meters, resembling a saturation pattern. Although inter-annual variability in landslide extent is reduced after spectral calibration, it still exceeds the spatial variability observed within a single year. Consequently, analyzing the first derivative is essential for revealing stable distance-based patterns in landslide distribution.

Based on the 2021 digitized aerial imagery, ground truth landslide polygons totaling approximately 25 ha were identified. These areas exhibited a mean soil fraction of 0.631, which was adopted as the threshold for detecting landslides in the AutoMCU outputs. Given the consistency of spatial patterns across years, the study further evaluates temporal changes in landslide activity within the 100-meter buffer zones surrounding each land use type (Figure 10). While differences between land use categories are relatively minor, all three show a clear peak in 2010, followed by a general decline from 2011 to 2021.

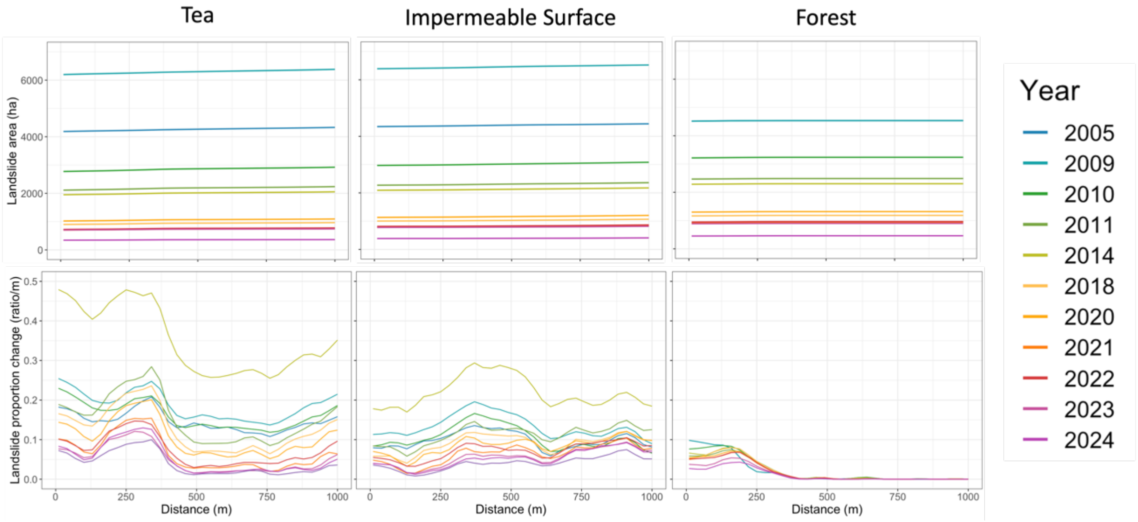

Figure 6. From left to right: tea plantations, impervious surfaces, and forests. The top

row shows the total soil area within buffer zones at varying distances for different years and land use types (calculated as the sum of soil proportions within each buffer). The bottom row presents the first derivative of the top-row data, illustrating the rate of change in soil area with increasing distance from the target land use type.

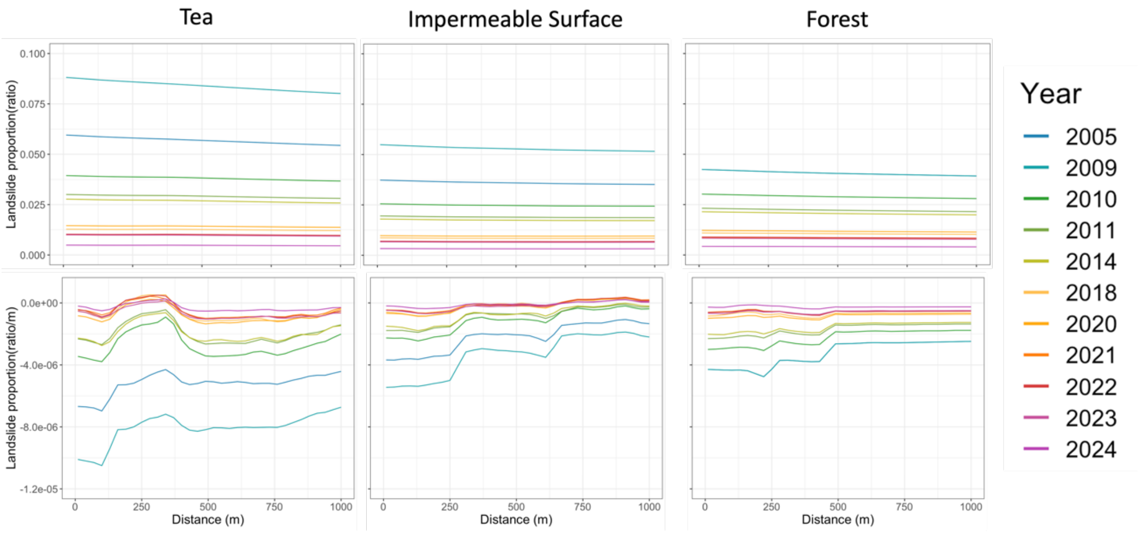

Figure 7. From left to right: tea plantations, impervious surfaces, and forests. The top row shows the proportion of soil area within the total buffer area at varying distances for different years and land use types. The bottom row presents the first derivative of the top row data, indicating the rate of change in soil proportion with increasing distance from each land use type.

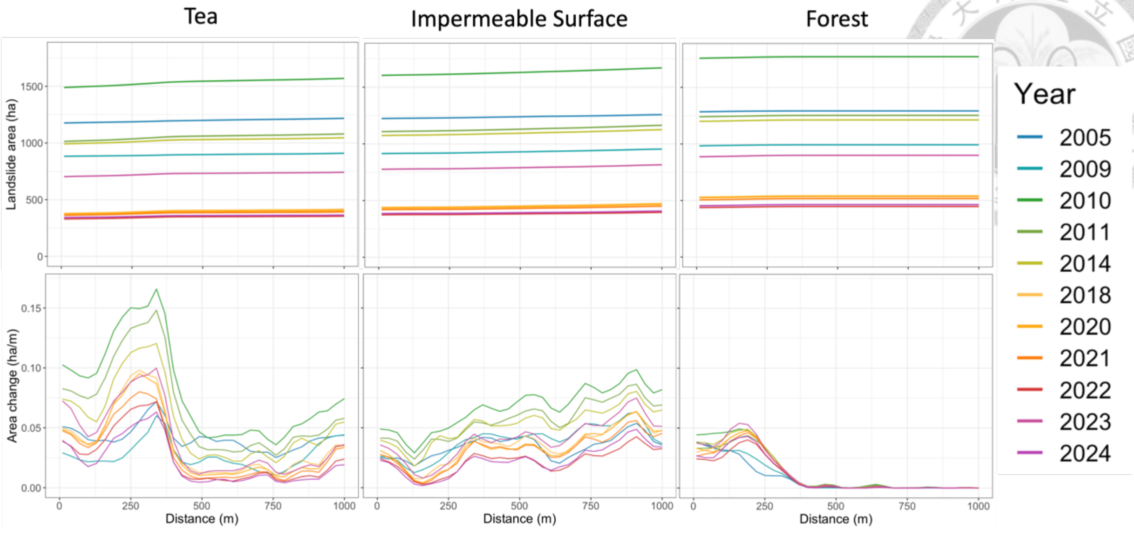

Figure 8. The results indicate that the estimated landslide area significantly decreased after spectral calibration. However, the first derivative patterns remain consistent with those before calibration, showing similar trends in landslide distribution relative to distance.

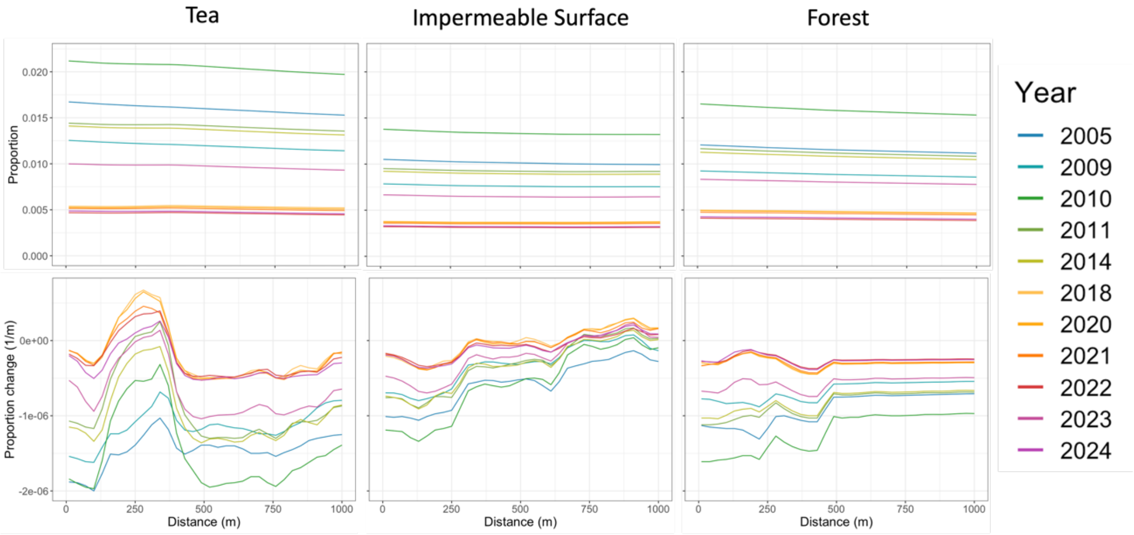

Figure 9. From left to right: tea plantations, impervious surfaces, and forests. The top row shows the proportion of soil area within the total buffer area at varying distances after spectral calibration. The bottom row presents the first derivative of the top row data, indicating the rate of change in soil proportion with increasing distance from each

land use type. Compared with Figure 8 (before calibration), Figure 10 reveals the impact of spectral calibration on soil fraction estimation. While the overall spatial trends remain consistent across land use types, the calibrated results show noticeably lower soil proportions. This suggests that the original (uncalibrated) AutoMCU results may have overestimated soil exposure, and that spectral calibration helps produce more conservative and possibly more accurate estimates.

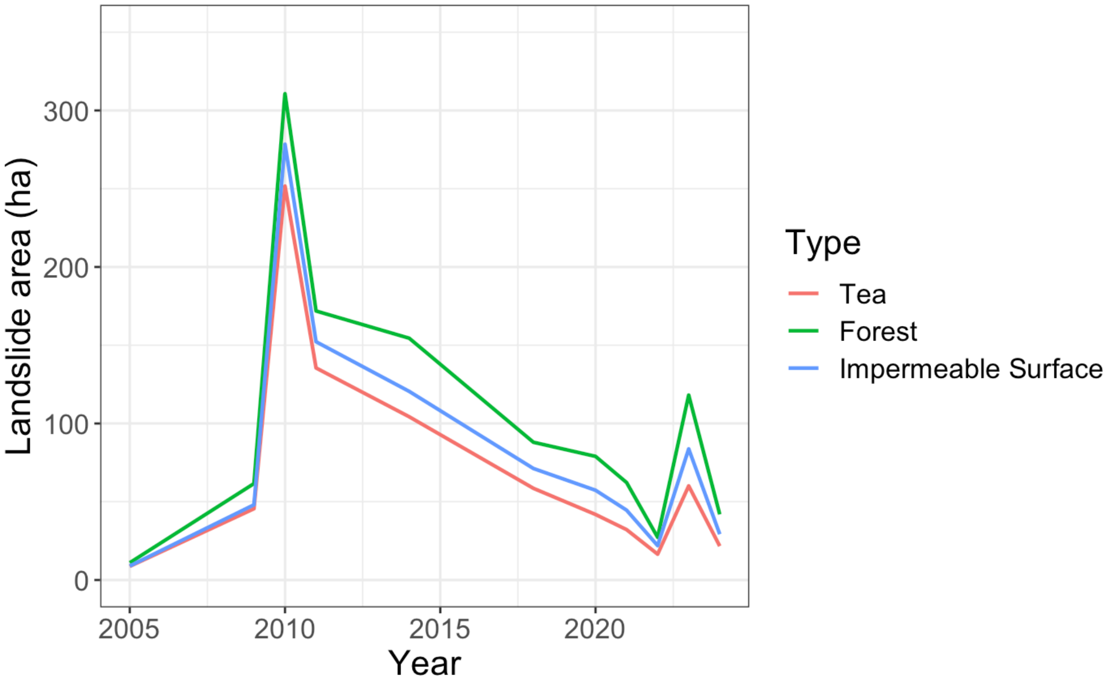

Figure 10. Temporal trends of landslide areas within 100-meter buffer zones of tea plantations, impermeable surfaces, and forests from 2005 to 2024. Landslide extent was consistently highest near forests, intermediate near impermeable surfaces, and lowest near tea plantations. A pronounced peak occurred in 2010, likely linked to extreme rainfall events, followed by a steady decline until 2021, with only a minor rebound in recent years.

doi:10.6342/NTU202504349

3.5 Topographic Analysis

Given that the most significant number of landslides occurred in 2010 according to this study's results, the 2010 AutoMCU output was used as the basis for analyzing the distribution of slope, aspect, and the landslide area within 10 meters of different land use types (Figure 11). The top row of the figure presents the total landslide area within the buffer zone. In contrast, the bottom row shows the total area normalized by the perimeter of each polygon, thereby reducing the bias caused by larger land parcels having more surrounding landslide area simply due to their size. The results indicate that, after normalization by perimeter, the differences in surrounding landslide area among different land-use types are no longer statistically significant.

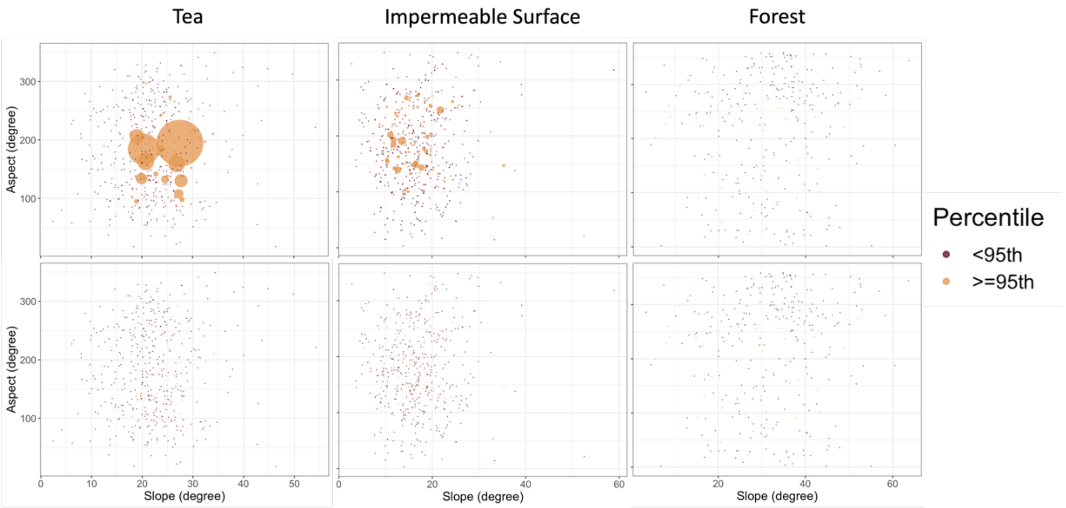

Figure 11. (Top row) Distribution of slope, aspect, and surrounding landslide area for tea plantations, impervious surfaces, and forests. (Bottom row) Landslide area normalized by the perimeter of each polygon. The landslide area is represented by the size of the circles, with lighter-colored circles indicating polygons that fall within the top 5% of the landslide area for each land use category. The figure shows that while some tea plantations and impervious surfaces have noticeably larger adjacent landslide areas, once normalized by perimeter, no significant difference is observed among the

doi:10.6342/NTU202504349

land use types.

Chapter 4 Discussion

4.1 Land use and land cover

The land use and land cover (LULC) classification produced high overall accuracy, particularly in distinguishing between forest and tea plantation areas—two categories that are often spectrally similar in optical imagery. This ability of identification represents a notable improvement over traditional pixel-based classification methods (Qu et al., 2022; Wang et al., 2018).

We attribute this enhanced performance to the use of the U-Net deep learning architecture, which is particularly effective in identifying spatial texture and contextual patterns (Karabağ et al., 2019). Unlike conventional classifiers such as Random Forest or Support Vector Machines, U-Net's encoder–decoder structure with skip connections enables it to preserve fine-scale spatial detail and resolve boundaries more precisely (Ronneberger et al., 2015). This structure is especially valuable in complex, mountainous landscapes like our study area, where tea plantations often intermingle with natural forests.

Moreover, the use of multi-seasonal Sentinel-2 imagery (10 m spatial resolution) helped reduce confusion caused by temporary spectral similarities, such as seasonal variations in vegetation (Khatami et al., 2016). The model's ability to integrate both spectral and spatial information enabled improved classification robustness and more accurate mapping of heterogeneous land cover types.

Overall, the results demonstrate that deep learning-based approaches, when combined with appropriate remote sensing data and seasonal compositing, can substantially improve the accuracy and reliability of LULC classification in highland

doi:10.6342/NTU202504349

agricultural regions.

4.2 Landslides

The results of this study demonstrate that integrating AutoMCU with MODIS-based spectral calibration provides a practical framework for monitoring landslide dynamics in complex mountainous environments. By applying cross-sensor spectral correction to Landsat imagery, the temporal consistency of reflectance data was significantly improved, reducing artificial variation caused by differing atmospheric conditions and sensor characteristics. This calibration step was crucial for ensuring the comparability of annual AutoMCU results, particularly in identifying year-to-year fluctuations in soil exposure related to landslide activity (Bosch et al., 2014; Chander et al., 2013).

Through the use of AutoMCU, sub-pixel fractions of PV, NPV, and soil were estimated, allowing for the detection of gradual or spatially diffuse changes in surface conditions. This approach was particularly valuable in areas with mixed land cover and steep topography, where traditional classification methods often fail to resolve subtle shifts in bare ground or erosion extent (Jafarzadeh & Hasanlou, 2019; Kressler & Steinnocher, 1999; Rashed et al., 2006). The temporal patterns of the soil endmember closely aligned with known extreme events, such as Typhoon Morakot in 2009, validating the method’s sensitivity to disturbance-driven landslide processes.

Moreover, the incorporation of buffer analysis provided spatial insights into landslide risk in relation to surrounding land use types. Results indicated that areas adjacent to tea plantations exhibited the highest proportion of soil (Figure 10), potentially due to the infrastructure commonly associated with tea cultivation. However,

doi:10.6342/NTU202504349

when examining actual landslide distribution (Figure 12), the results did not indicate a consistent increase in landslide activity around tea plantations compared to other land use categories. Instead, landslide-prone areas were most concentrated within 300–400 meters of both tea plantations and forests. This pattern suggests a spatial association between mountainous agriculture and landslides, though not necessarily a causal one. After spectral calibration, the inter-annual trends became more stable, reinforcing that the spatial patterns observed were not artifacts of sensor inconsistency.

In summary, the combination of AutoMCU, spectral calibration, and spatial analysis provided a coherent and sensitive approach for monitoring landslide dynamics over time. This framework not only captured short-term disturbance events but also revealed longer-term landscape recovery and interactions with land use.

4.3 The relationships between tea plantations and landslides

According to our initial hypothesis, we expected landslide occurrence to increase over time, even if the total area of tea plantations remained relatively stable. This assumption was based on previous research suggesting that highland agriculture—particularly long-term cultivation on steep terrain—can exacerbate slope instability through cumulative impacts such as soil compaction, root weakening, and hydrological alterations (Gu et al., 2019; Hou et al., 2018).

However, the results of this study did not fully support this expectation. While some spatial association between tea plantations and landslide-prone areas was observed—particularly within 400 meters of plantation boundaries—there was no consistent upward trend in landslide extent over time in areas adjacent to tea farms.

doi:10.6342/NTU202504349

Post-2010, the estimated soil fraction (a proxy for landslides) in these regions generally declined.

Several possible explanations may account for this discrepancy. One possibility is that high-mountain tea plantations in Taiwan have entered a relatively mature phase of development. The establishment of these plantations is capital-intensive, often requiring land leveling, terrace construction, retaining walls, drainage systems, and road access (Papaskiri et al., 2019). This substantial initial investment may motivate tea farmers to adopt more effective slope management practices, thereby safeguarding their long-term returns. Such practices—such as maintaining vegetative cover between rows, installing drainage channels, and avoiding over-expansion—can help reduce the likelihood of landslide initiation around plantations.

Second, this region may have benefited from post-disaster rehabilitation efforts following extreme events, such as Typhoon Morakot in 2009. Restoration activities and stricter land use regulations introduced in subsequent years could have helped reduce slope disturbance and improve overall stability in tea-growing areas.

Overall, while the spatial proximity between tea plantations and landslides remains evident, our temporal analysis suggests that under proper management and with minimal expansion into new terrain, high-mountain tea cultivation does not necessarily lead to a progressive increase in landslide occurrence. This finding underscores the importance of considering land management practices, not just land cover type, when assessing landslide risk in mountainous agricultural systems.

4.4 Potentials and limitations

This study demonstrates the potential of combining AutoMCU, spectral calibration,

doi:10.6342/NTU202504349

and spatial buffer analysis as a framework for long-term landslide monitoring in mountainous agricultural regions. By extracting sub-pixel soil fractions from medium-resolution imagery, AutoMCU captures surface changes that traditional classification methods may overlook. The integration of MODIS-based cross-sensor calibration further improves temporal consistency, enabling more reliable comparison across years and satellite platforms. Additionally, the buffer analysis effectively highlights spatial patterns in landslide occurrence relative to different land-use types, offering insights into landscape-level interactions between human activity and geomorphic processes.

Despite these strengths, several limitations should be acknowledged. First, while spectral calibration reduces inter-annual variability, some residual bias—particularly in earlier Landsat imagery—remains due to differences in sensor aging, image quality, and the limited availability of stable reference targets. Second, the AutoMCU method depends heavily on the representativeness and stability of selected endmembers. In areas with high spectral heterogeneity or partial cloud contamination, fractional estimates may be less reliable. Third, this study focuses primarily on exposed soil as a proxy for landslides. Shallow landslides covered by vegetation, or subsurface movements, may not be captured using this approach.

Additionally, our analysis does not incorporate external factors such as rainfall intensity, typhoon paths, slope gradient, or land management practices, all of which could influence landslide initiation and recovery. Including these variables in future models—potentially through machine learning or multi-source data fusion—could enhance explanatory power and predictive capacity. Finally, while buffer analysis reveals spatial proximity patterns, it does not confirm causality. More targeted field validation and high-resolution temporal analysis would be needed to assess the direct

doi:10.6342/NTU202504349

influence of specific agricultural activities on slope stability.

In summary, while the proposed method provides a robust starting point for understanding landslide dynamics in tea plantation regions, continued refinement—particularly in data integration and validation—is essential for advancing sustainable land management in high-risk mountainous environments.

doi:10.6342/NTU202504349

Chapter 5 Conclusions

This study demonstrates the applicability of satellite-based approaches for monitoring land use and landslide dynamics in mountainous agricultural landscapes. By integrating seasonally composited Sentinel-2 imagery with a U-Net deep learning model, we successfully produced a high-accuracy land use classification map for the Greater Ali-Mountain tea plantation region. Combined with AutoMCU-based sub-pixel analysis of soil fractions from 2005 to 2022, this framework enabled the long-term tracking of landslide distribution and its relationship to land use.

The results reveal a general decline in landslide extent over the past two decades, with peaks corresponding to known extreme weather events. Importantly, despite the spatial proximity between landslide-prone areas and tea plantations, no clear long-term correlation was found between the extent of tea cultivation and the increased occurrence of landslides. This suggests that when properly managed—with stable site selection and adequate slope protection—high-mountain tea farming may not significantly exacerbate landslide risk.

Overall, this study highlights the potential of medium-resolution satellite imagery, combined with spectral unmixing and spatial analysis techniques, to provide valuable insights into landscape processes at scale. The findings contribute to a growing body of research suggesting that agricultural impacts on slope stability depend as much on land management practices as on land cover type.

Future research will expand on these results by incorporating spatial statistical methods (e.g., spatial autocorrelation) and terrain variables (e.g., slope, aspect) to characterize landslide susceptibility further. Event-based landslide inventories will also

doi:10.6342/NTU202504349

be integrated to refine detection thresholds and improve the interpretability of AutoMCU outputs. These advancements will enhance our ability to identify landslide hotspots and support sustainable land use planning in sensitive mountainous regions.

Chapter 6 References

內政部國土測繪圖資服務雲（2024）。正射影像圖（臺灣通用）。取自 https://maps.nlsc.gov.tw/S09SOA/homePage.action?Language=ZH 。

中華民國內政部國土測繪中心（2023）。土地利用分級分類 109 年以後。取自 https://ws.moi.gov.tw/Download.ashx?u=LzAwMS9VcGxvYWQvNDA3L3JlbGZpbGUvOTI3My8zMTkzLzIxOGM3MWI3LTU2NTctNDg4NC1hOWEyLTU1Zjk1MjhmOWFkNi5wZGY%3d&n=5Zyf5Zyw5Yip55So5YiG57Sa5YiG6aGe57O757Wx6KGo6Zm45Z%2bf6YOo5Lu9LnBkZg%3d%3d 。

農業部農糧署（2024）。農情報告資源網。取自 https://agr.afa.gov.tw/afa/afa_frame.jsp 。

Alimohammadlou, Y., Najafi, A., & Yalcin, A. (2013). Landslide process and impacts: A proposed classification method. *Catena*, *104*, 219-232.

Asner, G. P., & Lobell, D. B. (2000). A biogeophysical approach for automated SWIR unmixing of soils and vegetation. *Remote Sensing of Environment*, *74*(1), 99-112. https://doi.org/10.1016/s0034-4257(00)00126-7

Bosch, W., Dettmering, D., & Schwatke, C. (2014). This calibration step was crucial for ensuring the comparability of annual AutoMCU results, particularly in identifying year-to-year fluctuations in soil exposure related to landslide activity. *Remote Sensing*, *6*, 2255-2281. https://doi.org/10.3390/rs6032255

Chander, G., Hewison, T. J., Fox, N., Wu, X., Xiong, X., & Blackwell, W. J. (2013). Overview of Intercalibration of Satellite Instruments. *IEEE Transactions on Geoscience and Remote Sensing*, *51*(3), 1056-1080. https://doi.org/10.1109/TGRS.2012.2228654

Che, X., Zhang, H. K., & Liu, J. (2021). Making Landsat 5, 7 and 8 reflectance consistent using MODIS nadir-BRDF adjusted reflectance as reference. *Remote Sensing of Environment*, *262*. https://doi.org/10.1016/j.rse.2021.112517

Chen, C.-S., Chen, Y.-L., Liu, C.-L., Lin, P.-L., & Chen, W.-C. (2007). Statistics of Heavy Rainfall Occurrences in Taiwan. *Weather and Forecasting*, *22*(5), 981–1002. https://doi.org/10.1175/WAF1033.1

Chen, H., Dadson, S., & Chi, Y.-G. (2006). Recent rainfall-induced landslides and debris flow in northern Taiwan. *Geomorphology*, *77*, 112–125. https://doi.org/10.1016/j.geomorph.2006.01.002

Chen, P. H., Lin, R. H., Chiu, C. F., & Lin, Y. S. (2025). Mitigating low-temperature frost damage in Taiwan high-altitude tea cultivation: physiological insight and protective strategies. *Planta*, *261*(125), 19. https://doi.org/10.1007/s00425-025-04704-2

doi:10.6342/NTU202504349

Chen, Y., Jiang, Y., Duan, J., Shi, J., Xue, S., & Kakuda, Y. (2010). Variation in catechin contents in relation to quality of 'Huang Zhi Xiang' Oolong tea (Camellia sinensis) at various growing altitudes and seasons. *Food Chemistry*, *119*(2), 648-652. https://doi.org/10.1016/j.foodchem.2009.07.014

Costa, J. E., & Schuster, R. L. (1987). The formation and failure of natural dams . *87-392*. https://doi.org/10.3133/ofr87392

Digra, M., Dhir, R., & Sharma, N. (2022). Land use land cover classification of remote sensing images based on the deep learning approaches: a statistical analysis and review. *Arabian Journal of Geosciences*, *15*. https://doi.org/10.1007/s12517-022-10246-8

Dou, Q. (2019). Tea in Health and Disease. *Nutrients*, *11*(929), 4. https://doi.org/10.3390/nu11040929

FAO. (2022). *International tea market: market situation, prospects and emerging issues*.

Garcia-Chevesich, P., Wei, X., Ticona, J., Martínez, G., Zea, J., García, V., Alejo, F., Zhang, Y., Flamme, H., Graber, A., Santi, P., McCray, J., Gonzáles, E., & Krahenbuhl, R. (2021). The Impact of Agricultural Irrigation on Landslide Triggering: A Review from Chinese, English, and Spanish Literature. *Water*, *13*(10). https://doi.org/10.3390/w13010010

Gariano, S. L., & Guzzetti, F. (2016). Landslides in a changing climate. *Earth-Science Reviews*, *162*, 227-252. https://doi.org/10.1016/j.earscirev.2016.08.011

Garwood, N. C., Janos, D. P., & Brokaw, N. (1979). Earthquake-Caused Landslides: A Major Disturbance to Tropical Forests. *Science*, *205*(4410), 997-999. https://doi.org/10.1126/science.205.4410.997

GDAL/OGR contributors. (2024). GDAL/OGR Geospatial Data Abstraction software Library. https://doi.org/10.5281/zenodo.5884351

Geertsema, M., Highland, L., & Vaugeouis, L. (2009). Environmental Impact of Landslides. In K. Sassa & P. Canuti (Eds.), *Landslides – Disaster Risk Reduction* (pp. 589-607). Springer Berlin Heidelberg. https://doi.org/10.1007/978-3-540-69970-5_31

Gorelick, N., Hancher, M., Dixon, M., Ilyushchenko, S., Thau, D., & Moore, R. (2017). Google Earth Engine: Planetary-scale geospatial analysis for everyone. . *Remote Sensing of Environment*. https://doi.org/10.1016/j.rse.2017.06.031

Gu, T.-f., Zhang, M.-s., Wang, J.-d., Wang, C.-x., Xu, Y.-j., & Wang, X. (2019). The effect of irrigation on slope stability in the Heifangtai Platform, Gansu Province, China. *Engineering Geology*, *248*, 346-356. https://doi.org/10.1016/j.enggeo.2018.10.026

Guariguata, M. R. (1990). Landslide Disturbance and Forest Regeneration in the Upper Luquillo Mountains of Puerto Rico. *Journal of Ecology*, *78*(3), 814-832. https://doi.org/https://doi.org/10.2307/2260901

Guennebaud, G., Jacob, B., & others. (2010). Eigen v3. http://eigen.tuxfamily.org. http://eigen.tuxfamily.org

Han, W., Huang, J., & Li, X. e. a. (2016). Altitudinal effects on the quality of green tea in east China: a climate change perspective. *European Food Research and Technology*, *243(2)*, 323-330. https://doi.org/https://doi.org/10.1007/s00217-016-2746-5

Han, W. Y., Huang, J. G., Li, X., Li, Z. X., Ahammed, G. J., Yan, P., & Stepp, J. R. (2017). Altitudinal effects on the quality of green tea in east China: a climate change perspective. *European Food Research and Technology*, *243*, 323-330. https://doi.org/10.1007/s00217-016-2746-5

Haq, S. u., & Boz, I. (2018). Developing a set of indicators to measure sustainability of tea cultivating farms in Rize Province, Turkey. *Ecological Indicators*, *95*(1), 219-232. https://doi.org/10.1016/j.ecolind.2018.07.041

He, K., Zhang, X., Ren, S., & Sun, J. (2015). Deep Residual Learning for Image Recognition. https://doi.org/10.48550/arXiv.1512.03385

Highland, L., & Bobrowsky, P. (2008). The Landslide Handbook – A Guide to Understanding Landslides.

Hou, X., Vanapalli, S. K., & Lia, T. (2018). Water infiltration characteristics in loess associated with irrigation activities and its influence on the slope stability in Heifangtai loess highland, China. *Engineering Geology*, *234*, 27-37. https://doi.org/10.1016/j.enggeo.2017.12.020

Huang, C., Chai, C., Chang, C., Huang, J., Hu, K., Lu, M., & Chung, Y. (2013). An Integrated Optical Remote Sensing System for Environmental Perturbation Research. *Ieee Journal of Selected Topics in Applied Earth Observations and Remote Sensing*, *6*(6), 2434-2444. https://doi.org/10.1109/jstars.2013.2250489

Imaizumi, F., Sidle, R. C., & Kamei, a. R. (2008). Effects of forest harvesting on the occurrence of landslides and debris flows in steep terrain of central Japan. *Earth Surface Processes and Landforms*, *33*. https://doi.org/10.1002/esp.1574

Jafarzadeh, H., & Hasanlou, M. (2019). An Unsupervised Binary and Multiple Change Detection Approach for Hyperspectral Imagery Based on Spectral Unmixing. *Ieee Journal of Selected Topics in Applied Earth Observations and Remote Sensing*, *12*(12). https://doi.org/10.1109/JSTARS.2019.2939133

Karabağ, C., Verhoeven, J., Miller, N. R., & Reyes-Aldasoro, C. C. (2019). Texture Segmentation: An Objective Comparison between Five Traditional Algorithms and a Deep-Learning U-Net Architecture. *Applied Sciences*, *9*(18). https://doi.org/10.3390/app9183900

Kelsey, H. M. (1978). Earthflows in Franciscan melange, Van Duzen River basin, California. *Geology*, *6*(6), 361-364. https://doi.org/10.1130/0091-7613(1978)6<361:EIFMVD>2.0.CO;2

Khatami, R., Mountrakis, G., & Stehman, S. V. (2016). A meta-analysis of remote sensing research on supervised pixel-based land-cover image classification processes: General guidelines for practitioners and future research. *Remote Sensing of Environment*, *177*, 89-100. https://doi.org/10.1016/j.rse.2016.02.028

Kjekstad, O., & Highland, L. (2009). Economic and Social Impacts of Landslides. In K. Sassa & P. Canuti (Eds.), *Landslides – Disaster Risk Reduction* (pp. 573-587). Springer Berlin Heidelberg. https://doi.org/10.1007/978-3-540-69970-5_30

Knapen, A., Kitutu, M. G., Poesen, J., Breugelmans, W., Deckers, J., & Muwanga, A. (2006). Landslides in a densely populated county at the footslopes of Mount Elgon (Uganda): Characteristics and causal factors. *Geomorphology*, *73*, 149–165. https://doi.org/https://doi.org/10.1016/j.geomorph.2005.07.004

Kressler, F. P., & Steinnocher, K. T. (1999). Detecting land cover changes from NOAA-AVHRR data by using spectral mixture analysis. *International Journal of Applied Earth Observation and Geoinformation*, *1*(1), 21-26. https://doi.org/10.1016/S0303-2434(99)85024-7

Lacroix, P., Dehecq, A., & Taipe, E. (2020). Irrigation-triggered landslides in a Peruvian desert caused by modern intensive farming. *Nature Geoscience*, *13*, 56-60. https://doi.org/10.1038/s41561-019-0500-x

Liu, W., Bai, R., Sun, X., Yang, F., Zhai, W., & Su, X. (2024). Rainfall- and Irrigation-Induced Landslide Mechanisms in Loess Slopes: An Experimental

Investigation in Lanzhou, China. *atmosphere*, *15*(162). https://doi.org/10.3390/atmos15020162

Microsoft. (2024). *Visual Studio Code*. In (Version 1.90.0)

Papaskiri, T. V., Peng, Y., Kasyanov, A. E., Semochkin, V. N., Ananicheva, E. P., & Volkov, I. V. (2019). Methods of land management when locating tea plantations. *Earth and Environmental Science*, *350*, 5. https://doi.org/10.1088/1755-1315/350/1/012067

Persichillo, M. G., Bordoni, M., & Meisina, C. (2017). The role of land use changes in the distribution of shallow landslides. *Science of the Total Environment*, *574*, 924–937. https://doi.org/10.1016/j.scitotenv.2016.09.125

Plafker, G., Ericksen, G. E., & Fernández Concha, J. (1971). Geological aspects of the May 31, 1970, Perú earthquake*. *Bulletin of the Seismological Society of America*, *61*(3), 543-578. https://doi.org/10.1785/bssa0610030543

Qu, L. a., Li, M., Chen, Z., Liu, W., Zhi, J., & Zhang, L. (2022). Mapping large area tea plantations using progressive random forest and Google Earth Engine. *Journal of Applied Remote Sensing*, *16*(2). https://doi.org/10.1117/1.JRS.16.024509

Rashed, T., Weeks, J. R., Stow, D., & Fugate, D. (2006). Measuring temporal compositions of urban morphology through spectral mixture analysis: toward a soft approach to change analysis in crowded cities. *International Journal of Remote Sensing 26*(4), 699-718. https://doi.org/10.1080/01431160512331316874

Ren, X., Lin, M., Liu, J., Khan, W., Zhao, H., Sun, B., Liu, S., & Zheng, P. (2025). Effects of Altitude on Tea Composition: Dual Regulation by Soil Physicochemical Properties and Microbial Communities. *Plants*, *14*(1642). https://doi.org/10.3390/plants14111642

Ronneberger, O., Fischer, P., & Brox, T. (2015). U-Net: Convolutional Networks for Biomedical Image Segmentation. https://doi.org/10.48550/arXiv.1505.04597

Schuster, R. L., & Highland, L. M. (2001). Socioeconomic and environmental impacts of landslides in the Western Hemisphere. *2001-276*, 47. https://doi.org/10.3133/ofr01276

Schuster, R. L., & Highland, L. M. (2007). Overview of the Effects of Mass Wasting on the Natural Environment. *Environmental and Engineering Geoscience*, *13*(1), 25-44. https://doi.org/10.2113/gseegeosci.13.1.25

Statista. (2025). *Tea - Worldwide*. https://www.statista.com/outlook/cmo/hot-drinks/tea/worldwide

Team, R. C. (2024). *R: A language and environment for statistical computing.*

. In R Foundation for Statistical Computing. https://www.R-project.org/

Ungar, S. G., Pearlman, J. S., Mendenhall, J. A., & Reuter, D. (2003). Overview of the Earth Observing One (EO-1) mission. *IEEE Transactions on Geoscience and Remote Sensing*, *41*, 11. https://doi.org/10.1109/TGRS.2003.815999

Vanneste, M., Mienert, J., & Bünz, S. (2006). The Hinlopen Slide: A giant, submarine slope failure on the northern Svalbard margin, Arctic Ocean. *Earth and Planetary Science Letters*, *245*(1-2), 373-388.

Wang, Li, J., Jin, X., & Xiao, H. (2018). Mapping Tea Plantations from Multi-seasonal Landsat-8 OLI Imageries Using a Random Forest Classifier. *Journal of the Indian Society of Remote Sensing*, *47*(8), 1315–1329. https://doi.org/10.1007/s12524-019-01014-5

Wang, R., Gamon, J. A., Cavender-Bares, J., Townsend, P. A., & Zygielbaum, A. I. (2018). The spatial sensitivity of the spectral diversity–biodiversity relationship:

an experimental test in a prairie grassland. *Ecological Applications*, *28*(2), 541-556. https://doi.org/10.1002/eap.1669

Wu, C. D., & Wei, G. (2009). *19 - Tea as a functional food for oral health*. Woodhead Publishing. https://doi.org/10.1533/9781845696290.2.396

Xu, W., Song, Q., Li, D., & Wan, X. (2012). Discrimination of the Production Season of Chinese Green Tea by Chemical Analysis in Combination with Supervised Pattern Recognition. *Journal of Agricultural and Food Chemistry*, *60*(28), 7064−7070. https://doi.org/dx.doi.org/10.1021/jf301340z

Yanites, B. J., Mitchell, N. A., Bregy, J. C., Carlson, G. A., Cataldo, K., Holahan, M., Johnston, G. H., Nelson, A., Valenza, J., & Wanker, M. (2018). Landslides control the spatial and temporal variation of channel width in southern Taiwan: Implications for landscape evolution and cascading hazards in steep, tectonically active landscapes. *Earth Surface Processes and Landforms*, *43*, 1782–1797. https://doi.org/10.1002/esp.4353

Zhao, C., & Lu, Z. (2018). Remote Sensing of Landslides—A Review. *Remote Sensing*, *10*(279). https://doi.org/10.3390/rs10020279

doi:10.6342/NTU202504349

Chapter 7 Appendix

Table 3. Comparison of Sentinel-2 optical bands

This table lists Bands B2, B3, B4, B8, B11, and B12 of Sentinel-2. According to the European Space Agency (https://www.esa.int), the two satellites have similar spectral characteristics and the same spatial resolution for corresponding bands. Sentinel-2A has been operational since 2015, while Sentinel-2B has been in service since 2017.

Bands/ Satellite	Sentienl-2 A	Sentienl-2 B		
Cycle (days)	10	10		
Band number	Equivalent wavelength (nm)	Equivalent wavelength (nm)	Bandwidth (nm)	Spatial resolution
B2 (Blue)	496.6	492.1	65	10
B3 (Green)	560	559	35	10
B4 (Red)	664.5	665	30	10
B8 (NIR)	835.1	833	115	10
B11 (SWIR1)	1613.7	1610.4	90	20
B12 (SWIR2)	2202.4	2185.7	180	20

Table 4. Comparison of Optical Bands for Landsat Series Satellites

This table presents Bands B1 through B7 of the Landsat series. According to the U.S. Geological Survey (https://www.usgs.gov), although each Landsat satellite is equipped with different sensors, the observed spectral bands are similar and share the same spatial resolution. Landsat 5 was operational from 1984 to 2013, while Landsat 8 and Landsat 9 have been operating since 2013 and 2021, respectively.

Bands/ Satellite	Landsat 5	Bands/ Satellite	Landsat 8	
Cycle (days)	16	Cycle (days)	16	
Sensor	MSS/TM	Sensor	OLI/TIRS	
Band number	Equivalent wavelength (nm)	Band number	wavelength (nm)	Spatial resolution
		B1 (Ultra blue)	435-451	30 m
B1 (Blue)	450-520	B2 (Blue)	452-512	30 m
B2 (Green)	520-600	B3 (Green)	533-590	30 m
B3 (Red)	630-690	B4 (Red)	636-673	30 m
B4 (NIR)	770-900	B5 (NIR)	851-879	30 m
B5 (SWIR1)	1550-1750	B6 (SWIR1)	1566-1651	30 m
B7 (SWIR2)	2080-2350	B7 (SWIR2)	2107-2294	30 m
Bands/ Satellite	Landsat 9			
Cycle (days)	16			
Sensor	OLI/TIRS			
Band number	wavelength (nm)	Spatial resolution		
B1 (Ultra blue)	430-450	30 m		
B2 (Blue)	450-510	30 m		
B3 (Green)	530-590	30 m		
B4 (Red)	640-670	30 m		
B5 (NIR)	850-880	30 m		
B6 (SWIR1)	1570-1650	30 m		
B7 (SWIR2)	2110-2290	30 m		